

¹ **The effect of finite pore length on ion structure and charging**

² Konrad Breitsprecher,¹ Manuel Abele,¹ Svyatoslav Kondrat,^{1,2} and Christian Holm¹

³ *¹Institute for Computational Physics, Universität Stuttgart,*

⁴ *Allmandring 3, D-70569 Stuttgart, Germany*

⁵ *²Institute of Physical Chemistry, Polish Academy of Sciences,*

⁶ *Kasprzaka 44/52, 01-224 Warsaw, Poland*

Nanoporous supercapacitors play an important role in modern energy storage systems, and their modeling is essential to predict and optimize the charging behaviour. Two classes of models have been developed that consist of finite and infinitely long pores. Here, we show that although both types of models predict qualitatively consistent results, there are important differences emerging due to the finite pore length. In particular, we find that the ion density inside a finite pore is not constant but increases linearly from the pore entrance to the pore end, where the ions form a strongly layered structure. This hinders a direct quantitative comparison between the two models. In addition, we show that although the ion density between the electrodes changes appreciably with the applied potential, this change has a minor effect on charging. Our simulations also reveal a complex charging behaviour, which is adsorption-driven at high voltages, but it is dominated either by co-ion desorption or by adsorption of both types of ions at low voltages, depending on the ion concentration.

⁷ **I. INTRODUCTION**

⁸ Electrical double-layer capacitors, or supercapacitors, are an important player on the
⁹ market of energy storage devices. Supercapacitors store energy by electrosorption of counter-
¹⁰ charge into the porous electrodes and provide high power densities and cyclability, but
¹¹ the stored energies are relatively low [1, 2]. To increase the energy storage, electrodes
¹² with *subnanometer* pores are used, which show anomalously high capacitances (per surface
¹³ area) [3–5] and hence high stored energies [6]. This anomalous increase of capacitance is due
¹⁴ to the emergence of a *superionic state* [7, 8], *i.e.*, screening of the electrostatic interactions in

¹⁵ narrow conducting pores [9–11]. In this work we shall focus on electrodes with such narrow
¹⁶ pores only.

¹⁷ Modelling plays a crucial role in understanding and predicting the properties of super-
¹⁸ capacitors, such as capacitance, energy storage and charging times. There have been many
¹⁹ models and methods developed, but they can be conventionally split into two classes. One
²⁰ class consists of models that literally ‘mimic’ a supercapacitor, *i.e.*, they consider an ionic liq-
²¹ uid confined between two electrodes with porous structures, either with slit-shaped [12–16] or
²² cylindrical [12, 17] pores, or even featuring a complex pore network [18, 19]. However, since
²³ (typically molecular dynamics) simulations of such models are computationally demanding,
²⁴ they are necessarily ‘scaled-down’ as compared to their experimental counterparts. For in-
²⁵ stance, the pore length in a typical simulation is tens of nanometers at best, while in the
²⁶ experimental systems the pores can be micrometer long, as follows from the carbon particle
²⁷ sizes (see, *e.g.*, Refs. [20, 21], and Ref. [22]); likewise, the size of the region between the
²⁸ electrodes is of the order of nanometers in simulations, but it is hundreds of micrometers or
²⁹ millimeters in real supercapacitors.

³⁰ On the other hand, there is a class of simplified models that consider an ionic liquid
³¹ confined to a *single* pore, either slit-shaped [7, 8, 23–28] or cylindrical [29–32]. These models
³² are likely to describe more closely the long pores of real porous electrodes [22], but their
³³ deficiency is that the effects related to the pore closing and opening are ignored and the
³⁴ charging dynamics are not straightforward to study. Often such simplified models can be
³⁵ treated analytically [7, 28–32], but also Monte Carlo (MC) simulations [8, 23–25, 32] and
³⁶ classical density functional theories [26, 27, 33] have been applied.

³⁷ The main goal of this work is to connect these two types of models and to study the effects
³⁸ of finite and infinite pore lengths on the ion structure and charging. To this end, we take a
³⁹ variation of the model of a single slit nanopore of infinite length developed in Refs. [7, 8].
⁴⁰ We shall also present a *new model* for supercapacitors, which consists of two electrodes with
⁴¹ slit nanopores; in contrast to other similar models [13–16], our model considers pores that
⁴² are open on one side only (*cf.* Fig. 1a), *i.e.*, we take into account the pore closings explicitly.
⁴³ We shall first show how the superionic state emerges in this model (Section II; in this section
⁴⁴ we also describe the details of both models and the methods used to study them). Then, we
⁴⁵ shall discuss how the parameters of the two models can be connected (Section III) and how
⁴⁶ to adjust the simulations and the analysis to make a meaningful comparison (Section IV).

⁴⁷ The results obtained by these two models are compared and discussed in Section V. In
⁴⁸ Section VI we discuss how the ion structure and charging behaviour depend on the pore
⁴⁹ wall-ion interactions. We summarize and conclude in Section VII.

50

II. MODELS AND METHODS

⁵¹ We compare two models of nanoporous supercapacitors. In one model we consider a
⁵² supercapacitor that consists of two electrodes separated by a distance H , with each electrode
⁵³ featuring a slit nanopore of the specified width w and *finite* length l (Fig. 1a). This model
⁵⁴ will be used in MD simulations as described below; we shall call it the MD model.

⁵⁵ In addition, we consider a model consisting of a single nanopore, *i.e.*, an ionic liquid
⁵⁶ confined between two parallel metal plates, which are *infinitely* extended in the lateral
⁵⁷ directions (Fig. 1b); this model will be treated by MC simulations and will be called the MC
⁵⁸ model henceforth. We apply a potential U at the plates of the MC model (see Section II C),
⁵⁹ which by symmetry corresponds to the applied potential $2U$ between the two electrodes of
⁶⁰ the MD model.

⁶¹ In both models and in all simulations, we shall use the same pore width $w = 9.37\text{\AA}$. We
⁶² note that the pore width accessible to the ions is smaller, as will be discussed below.

63

A. Ionic liquid

⁶⁴ In both MD and MC simulations, we have taken charged soft spheres to model an ionic
⁶⁵ liquid. The ion-ion soft potential was the repulsive-only Weeks-Chandler-Anderson (WCA)
⁶⁶ potential [34], ϕ_{WCA} . We recall that ϕ_{WCA} is the standard 12-6 Lennard-Jones potential
⁶⁷ cut at the ion-ion separation $R_{\min} = 2^{1/6}\sigma$, where σ is the ion diameter, and shifted such
⁶⁸ that $\phi_{\text{WCA}} = 0$ at $R = R_{\min}$; this is to ensure that the corresponding force is a continuous
⁶⁹ function of R .

⁷⁰ The following parameters have been used in all simulations: Interaction parameter $\epsilon =$
⁷¹ 1kJ/mol and the ion diameter $\sigma = \sigma_{\pm} = 5\text{\AA}$. In the solvent-free case, these parameters
⁷² give the pressure 1atm for the ion volume fraction 0.134 (molar concentration 0.6M) and at
⁷³ temperature $T = 400\text{K}$.

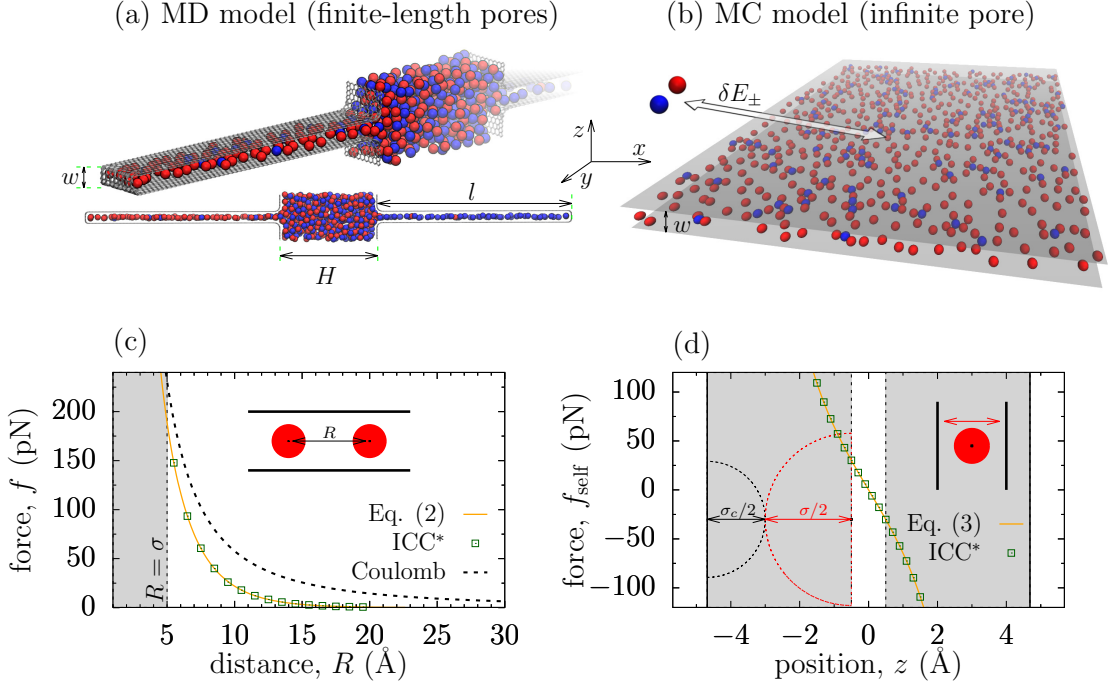


FIG. 1. Supercapacitor models in Monte Carlo (MC) and molecular dynamics (MD) simulations.

(a) In MD simulations an ionic liquid is confined between two electrodes with a slit pore of *finite* length each. The electrodes are constructed from the carbon atoms, and the electrostatic potential $2U$ is applied between the electrodes. (b) In Monte Carlo simulations the ions are confined in a single metallic slit pore, *infinitely* extended in the lateral directions. The electrostatic potential U is applied to the pore walls with respect to the bulk (*i.e.*, unconfined) electrolyte. (c) Force f between two ions confined in a metallic slit pore of width $w = 9.37\text{\AA}$. The open squares denote the force calculated by the ICC* method in the middle of a finite pore; this method is used for constant-potential MD simulations. The solid line shows the force obtained directly from the interaction potential for an *infinite* pore, Eq. (2), *i.e.*, $f_{\alpha\beta} = -dv_{\alpha\beta}/dR$ (note that $f_{++} = f_{--} = -f_{+-} \equiv f$). The ion diameters are $\sigma = \sigma_{\pm} = 5\text{\AA}$ and their centers are located on the symmetry plane of the slit, *i.e.*, $z_1 = z_2 = 0$ in Eq. (2). The Coulomb force (dash line) is shown for comparison. (d) Force f_{self} acting on a single ion inside a slit metallic pore due to image forces. The open squares show f_{self} calculated in the middle of a finite pore by using the ICC* method, which is compared with the force for the infinitely long pore, $f_{\text{self}} = -dE_{\text{self}}/dz$ obtained from the interaction potential (3) used in the MC simulations (solid line).

74

B. Pore walls

75 In the MD model the electrodes have been constructed from carbon atoms, which, how-
 76 ever, we modeled as WCA particles with the following parameters: $\sigma_c = 3.37\text{\AA}$ and
 77 $\epsilon_c = 1\text{kJ/mol}$. The hexagonal structure of the pore walls was obtained by subdividing
 78 the surface into equilateral triangles and placing the atoms in their centers. A side length
 79 of 2.5\AA provides an atom-atom bond length of 1.44\AA , similar as in graphene. The pore
 80 entrance was curved with a radius of 4\AA , and the pore closing was curved with a radius of
 81 2\AA .

In the MC model we neglect the pore wall structure and consider flat soft walls instead.
 To this end we propose the 10-4 Lennard-Jones (LJ) interaction potential

$$\phi_{\text{wall-ion}}^{\text{MC}}(z) = 2\pi\epsilon_{\text{wall-ion}}\sigma_{\text{wall-ion}}^2\rho_{\text{wall}} \left[\frac{2}{5} \left(\frac{\sigma_{\text{wall-ion}}}{z - z_0} \right)^{10} - \left(\frac{\sigma_{\text{wall-ion}}}{z - z_0} \right)^4 \right] \quad (1)$$

82 where $\epsilon_{\text{wall-ion}}$ and $\sigma_{\text{wall-ion}}$ are the wall-ion energy and diameter parameters, ρ_{wall} is the
 83 *two-dimensional* number density of carbon atoms, and z_0 is the location of the wall. This
 84 potential is obtained by integrating the LJ inter-particle interaction potential over a *surface*
 85 of LJ particles, where the surface is infinitely extended in the (x, y) directions.

86 In order to match the MC and MD models, we have fitted the interaction potential
 87 (1) to the *averaged* potential that an ion experiences when approaching an atomistic wall.
 88 We emphasize that (i) this fit is difficult to do accurately in the whole range of the wall-
 89 ion distances, and (ii) the atomistic wall-ion potential is not homogeneous in the lateral
 90 directions (Supplementary Fig. S1). We will discuss this in Section VI, where we also consider
 91 the case of hard pore walls with the accessible pore width $w_{\text{acc}} = 6\text{\AA}$ for comparison.

92

C. Grand canonical Monte Carlo simulations

93 In the MC model a slit pore is *infinitely* extended in the (x, y) directions (Fig. 1b), which
 94 is modeled by applying periodic boundary conditions in these directions. The electrostatic
 95 potential U was applied to the pore walls, which amounts to setting the electro-chemical
 96 potential to $\mu_{\pm} = \pm eU + \delta E_{\pm}$, where e is the elementary charge and δE_{\pm} is an energy of
 97 transfer of a \pm ion from the bulk of a supercapacitor into the pore (assumed equal for anions
 98 and cations). Note that δE does *not* include the change in the ion's self-energy (*cf.* Eq. (3)),

⁹⁹ and that its typical values lie between $-5k_B T$ and $45k_B T$ [35].

The electrostatic interaction energy between two ions confined in a metal slit pore is [7]

$$v_{\alpha\beta}(z_1, z_2, R) = \frac{4q_\alpha q_\beta}{\varepsilon w} \sum_{n=1}^{\infty} K_0(\pi n R/w) \sin(\pi n(z_1 + 1/2)/w) \sin(\pi n(z_2 + 1/2)/w) \quad (2)$$

¹⁰⁰ where q_α and q_β are the ion charges ($= \pm e$ in this work), R is the lateral distance between
¹⁰¹ the ions, $z_1, z_2 \in [-w/2, w/2]$ are their positions across the pore, and ε is the dielectric
¹⁰² constant (taken $\varepsilon = 4$ in this work).

An ion confined in a narrow conducting nanopore experiences an image-force attraction to the pore walls. For a slit metallic pore, infinitely extended in the lateral directions, this interaction energy can be calculated analytically [7]

$$E_{\text{self}}^{(\alpha)}(z) = -\frac{q_\alpha^2}{\varepsilon w} \int_0^\infty \left[\frac{1}{2} - \frac{\sinh(k(1/2 - z/w)) \sinh(k(1/2 + z/w))}{\sinh(k)} \right] dk, \quad (3)$$

¹⁰³ where z is the position across the pore. Note that $E_{\text{self}}^{(\alpha)}$ does not depend on the ion charge
¹⁰⁴ but only on its valency (taken 1 in this work); thus, we shall omit index α in $E_{\text{self}}^{(\alpha)}$.

¹⁰⁵ The interaction potentials (2) and (3) constitute the superionic state. They were imple-
¹⁰⁶ mented in towhee simulation package [8, 36] and grand canonical Monte Carlo simulations
¹⁰⁷ were performed using the Widom insertion-deletion move [37], translational move, and the
¹⁰⁸ molecular-type swap move [8]. We performed 5×10^6 equilibration runs and up to 10^7
¹⁰⁹ production runs at temperature $T = 400\text{K}$.

¹¹⁰

D. Molecular dynamics simulations

¹¹¹ MD simulations have been performed using ESPResSo simulation package [38–40] with
¹¹² the velocity-Verlet algorithm for integration and a Langevin thermostat (at temperature
¹¹³ $T = 400\text{K}$ and damping constant $\xi = 10\text{ps}^{-1}$) to model a NVT ensemble.

¹¹⁴ For constant potential simulations, we used the ICC* algorithm [41–43] in combination
¹¹⁵ with the 3D-periodic electrostatic solver P³M [44]. In the ICC* method, the induced ICC*
¹¹⁶ charges are defined on a discretized closed surface, and their values are determined iter-
¹¹⁷ atively each simulation step. Since the standard P³M solver does not take into account
¹¹⁸ the applied potential between the electrodes, we have additionally superimposed the cor-
¹¹⁹ responding external electrostatic potential, which has been pre-calculated numerically by

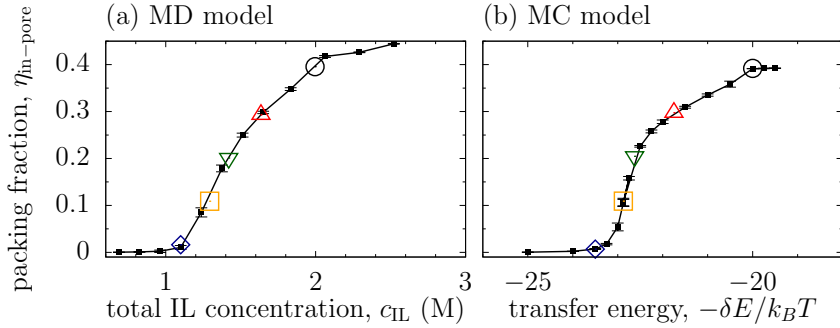


FIG. 2. Ion packing fraction in the pore at zero voltage from molecular dynamics (MD) and Monte Carlo (MC) simulations. (a) Ion packing fraction as a function of the total concentration c_{IL} of an ionic liquid (IL) from MD simulations. (b) Ion packing fraction in the pore from MC simulations as a function of δE , an energy of transfer of an ion from the bulk electrolyte into the pore. Large symbols (rhombus, square, up and down triangles and circle) show the systems taken for a comparison of MC and MD models (*cf.* Figs. 7 and 8).

¹²⁰ solving the Laplace equation with the appropriate boundary conditions; this has been done
¹²¹ iteratively on a equidistant lattice using a seven-point-stencil relaxation algorithm [45].

¹²² To test how the superionic state emerges within the ICC* approach, we have calculated
¹²³ the force between two ions in the pore middle, and compared it with the force obtained from
¹²⁴ Eq. (2) as $f_{\alpha\beta} = -dv_{\alpha\beta}/dR$ (note that $f_{++} = f_{--} = -f_{+-} \equiv f$). Figure 1c demonstrates an
¹²⁵ excellent agreement between the two methods. We have also compared the force due to image
¹²⁶ forces acting between an ion and the pore walls obtained by the ICC* approach and from
¹²⁷ Eq. (3) as $f_{\text{self}} = -E_{\text{self}}/dz$; again the agreement is very good (Fig. 1d). We note however
¹²⁸ that the corresponding *potential* acquires an additional contribution due to periodicity (see
¹²⁹ Supplementary Fig. S2), which can be corrected by considering larger systems. However,
¹³⁰ this shift in E_{self} does not influence the ion-pore walls *forces*, as Fig. 1d demonstrates, and
¹³¹ therefore the results of the MD simulations (*i.e.*, it only shifts the energy level, but the
¹³² energy differences remain the same).

¹³³

III. NON-POLARIZED NANOPORES

¹³⁴ In order to facilitate a comparison between the two models (Fig. 1a-b), we have matched
¹³⁵ the in-pore ion packing fractions at zero potential, $U = 0$. We calculated this packing

¹³⁶ fraction as $\eta_{\text{in-pore}} = \pi\sigma^3/(6\Omega)$, where $\sigma = \sigma_{\pm} = 5\text{\AA}$ is the ion diameter and $\Omega = Sw_{\text{acc}}$ is
¹³⁷ the volume of a pore; here S is the lateral area and w_{acc} the accessible pore width. In the MD
¹³⁸ model, unless otherwise specified, only the middle parts of the pores were taken into account
¹³⁹ when calculating $\eta_{\text{in-pore}}$, *i.e.*, the entrance and the closing of the pores were excluded (see
¹⁴⁰ Section IV A). Since w_{acc} is not known *a priori* and is expected to vary with the applied
¹⁴¹ potential, for definiteness we took $w_{\text{acc}} = w - \sigma_c$, where $\sigma_c = 3.37\text{\AA}$ is the diameter of the
¹⁴² carbon atom. The pore width $w = 9.37\text{\AA}$ gives $w_{\text{acc}} = 6\text{\AA}$. Note that this is the accessible
¹⁴³ pore width for a system with hard pore walls.

¹⁴⁴ In the MC model, the pore occupation is controlled by the ion transfer energy $\delta E_{\pm} = \delta E$.
¹⁴⁵ Figure 2a shows that the in-pore packing fraction decreases as δE increases, and the pore
¹⁴⁶ becomes more ionophobic [35, 46].

¹⁴⁷ In the MD model, the in-pore ion packing fraction can be controlled by changing the total
¹⁴⁸ concentration of ions in a supercapacitor, c_{IL} . Physically this can be realized by varying the
¹⁴⁹ pressure in the case of neat ionic liquids or by varying the salt concentration in the case
¹⁵⁰ of electrolyte solutions. Figure 2b demonstrates that the pore becomes less populated as
¹⁵¹ c_{IL} decreases. However, at extremely low concentrations our MD simulations predict the
¹⁵² formation of ionic liquid clusters in the bulk electrolyte (*i.e.*, between the electrodes), which
¹⁵³ influence the charging behaviour; we have therefore decided not to consider such cases in
¹⁵⁴ this work.

¹⁵⁵ After having matched the pore occupancies at no applied potential, we perform voltage-
¹⁵⁶ dependent MC and MD simulations for the systems shown by symbols in Fig. 2.

¹⁵⁷ IV. CHARGING OF NANOPORES OF FINITE LENGTH (MD MODEL)

¹⁵⁸ There are two important parameters in the MD model that are not present in our MC
¹⁵⁹ system, *viz.* the pore length l and the size H of the bulk of a supercapacitor. In order to
¹⁶⁰ understand better their potential impact on charging, we first discuss how they influence
¹⁶¹ the structure of an ionic liquid, in comparison to the MC model of a single infinitely-long
¹⁶² nanopore.

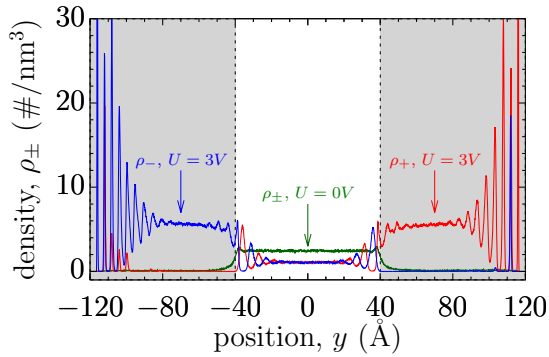


FIG. 3. Ion density profiles ρ_{\pm} from MD simulations. The green line shows $\rho_+ = \rho_-$ at no voltage, and the blue and red lines show ρ_+ and ρ_- at applied potential $U = 3V$. The grey areas denote the location of the pores. Without the appropriate correction steps, the co-ions get trapped in the pores, and the density of ions in the bulk electrolyte between the electrodes depends on the applied voltage. The total concentration of an ionic liquid in the supercapacitor is $c_{IL} \approx 1.1M$.

163

A. Ion structure

164

Figure 3 shows the average ion density profiles $\rho_{\pm}(y)$ between the two electrodes for zero and non-zero applied potentials. We can make the following observations:

166

1. The average ion density in the bulk electrolyte depends on the applied voltage. This implies that the chemical potential of the bulk ionic liquid changes with voltage, while it is taken constant in the MC model.
2. Some *co-ions* become trapped near the pore closings on the time scales of our MD simulations. This means that the system has not reached equilibrium. Note that this is unlikely to happen in the MC model as we perform grand canonical simulations.
3. The ions exhibit a clear layering near the pore closings and openings, while they seem to form a nearly homogeneous structure in the middle of a pore. However, for non-zero potentials the counter-ion density *is not constant along the pore* and increases from the pore entrance to the pore end. Clearly, in the MC model the average ion densities are position independent.

177

We shall now discuss how to correct the MD simulations to be able to approach more closely the single-pore supercapacitor models. We will see, however, that although points

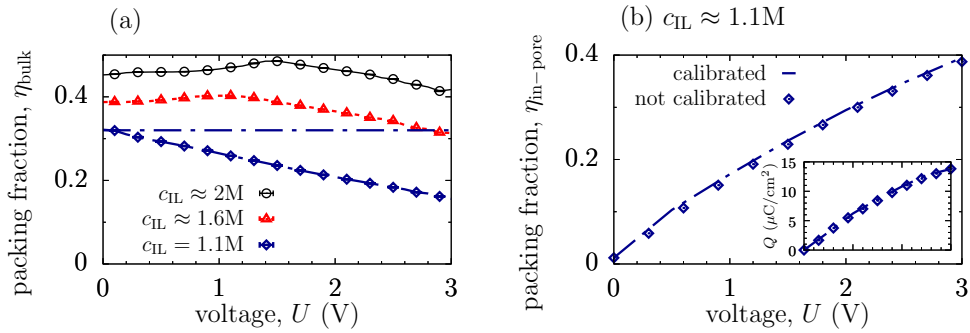


FIG. 4. Calibration of bulk density in MD simulations. (a) Total packing fraction η_{bulk} of the ions in the *bulk* electrolytes between the electrodes (see Fig. 1a); η_{bulk} can change significantly with the applied potential. To keep η_{bulk} constant (dash-dot line for $c_{\text{IL}} \approx 1.1\text{M}$) we calibrate the bulk density during equilibration runs by inserting ion pairs into the system (see the main text). (b) Total packing fraction $\eta_{\text{in-pore}}$ of the ions in the pore with and without density calibration for $c_{\text{IL}} = 1.1\text{M}$; for the remaining two concentrations from panel (a) see Supplementary Fig. S4. Such a calibration influences $\eta_{\text{in-pore}}$, albeit weakly, but its effect on the accumulated charge is negligible, however (see the inset).

¹⁷⁹ (1) and (2) can be corrected relatively easily, point (3) is more subtle and makes it difficult
¹⁸⁰ to compare the MC and MD models *quantitatively*.

¹⁸¹

B. Bulk density calibration

¹⁸² Clearly, also in experimental systems and commercially fabricated supercapacitors, the
¹⁸³ ion density in the bulk (*i.e.*, between the supercapacitor electrodes) can vary with the
¹⁸⁴ applied voltage. However, the volume of a bulk region in these systems is typically large,
¹⁸⁵ as compared to the total pore volume, and this change is expected to be small. In MD
¹⁸⁶ simulations, the size of a bulk region (H) is often comparable to the pore size [13–16], and
¹⁸⁷ its effect on the bulk density can therefore be significant (Fig. 4a).

¹⁸⁸ One way to deal with this problem is to consider systems with sufficiently large H ,
¹⁸⁹ which would, however, increase the computational costs accordingly. We have therefore
¹⁹⁰ taken a different route. We chose to *calibrate* the total number of ions in a system during
¹⁹¹ equilibration runs each time the voltage is changed. This was done by inserting ion pairs
¹⁹² into the system (or removing them from the system when necessary) until the bulk density

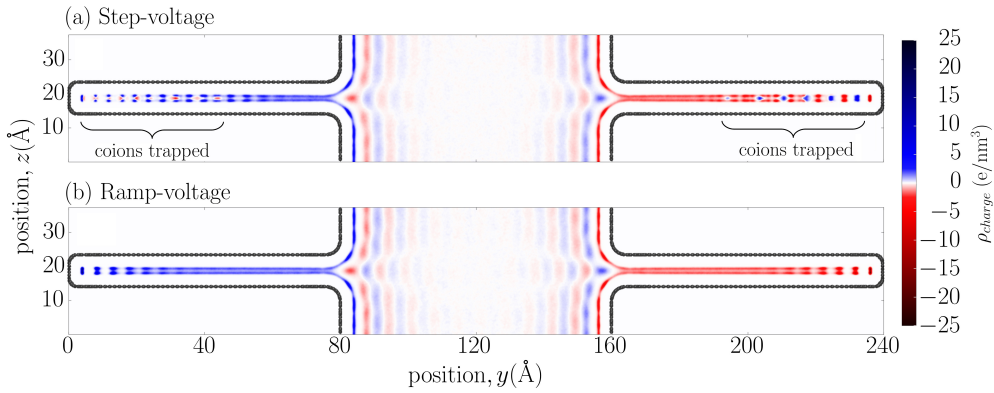


FIG. 5. Co-ion trapping in MD simulations. (a) Charge density heat-map for a step-voltage charging when a voltage of $2U = 6\text{V}$ is abruptly applied between the electrodes. Some co-ions are trapped near the pore closings even after 40ns of simulation time. (b) Co-ion trapping can be avoided by charging the system slowly with a linear voltage ramp $U(t) = kt$, where $k = 0.25\text{V/ns}$. There are no co-ions trapped in the pores after 10ns of simulation time. These plots show the simulation results averaged over the last 8ns of a 40ns simulation.

¹⁹³ $\rho_{bulk}(U \neq 0)$ equilibrates to $\rho_{bulk}(U = 0)$. After the calibration we run production runs as
¹⁹⁴ usual.

¹⁹⁵ Surprisingly at first glance, we have found that although the total ion density in the pore
¹⁹⁶ is slightly altered by calibration, it has practically no effect on the charge storage (Fig. 4b).
¹⁹⁷ This is likely because a change $\Delta\mu_{\pm}$ in the chemical potential due to the change in the
¹⁹⁸ ion density is small compared to what the system gains from the applied potential, *i.e.*,
¹⁹⁹ $\Delta\mu_{\pm} \ll eU$. We could not accurately estimate $\Delta\mu_{\pm}$ for our system, but we expect it to be
²⁰⁰ of the order of few $k_B T$'s [47]. This is supported by an observation that the change in the
²⁰¹ transfer energy of about $3k_B T$ (in the MC model) corresponds to the change in the total
²⁰² ion concentration from 1M to more than 2M (see Fig. 2). For comparison, $eU \approx 30k_B T$ at
²⁰³ $T = 400\text{K}$ and at an applied potential of 1V.

²⁰⁴

C. Avoiding ion trapping

²⁰⁵ Figures 3 and 5a show that at high voltages the co-ions in the pore become ‘trapped’ near
²⁰⁶ the pore closing on the time scales of our MD simulations ($\sim 100\text{ns}$). Such a co-ion trapping
²⁰⁷ leads to a decreased charge storage and sluggish dynamics [48]. To avoid ion trapping in

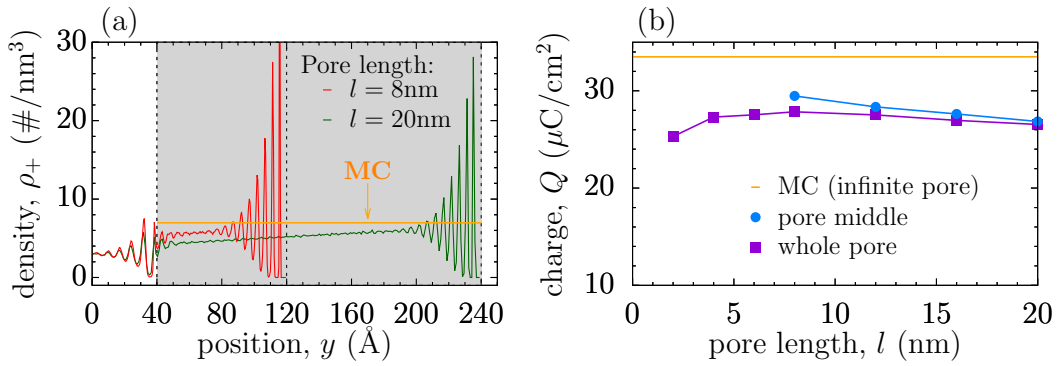


FIG. 6. Effect of pore length on ion structure and charging. (a) Counter-ion densities from MD simulations for different pore lengths l at applied potential $U = 3\text{V}$ (there are no coions in the pore at this voltage). The horizontal orange line shows the corresponding MC result. The MD results have been obtained using bulk calibration and ramp-voltage charging with the rate $k = 0.25\text{V/ns}$. The grey areas highlight the location of the pores, and the vertical dash lines show the pore entrance and closings. Only half of a supercapacitor is shown. (b) Accumulated charge per surface area as a function of pore length. The charge has been calculated for the whole pore and when only the middle part of a pore is taken into account (2nm from the pore entrance and 3.5nm from the pore end). The total concentration of an ionic liquid in the supercapacitor is $c_{\text{IL}} \approx 1.6\text{M}$ and the transfer energy in MC simulations is $\delta E = 21.75k_B T$. These parameters have been chosen such that the MC and MD models give the same ion densities at no applied voltage (see Fig. 2).

208 this work we have used a linear *voltage ramp* $U(t) = kt$ to charge our system, instead of a
 209 typically used step-voltage charging as in Fig. 5a. Figure 5b demonstrates that this strategy
 210 allows us to avoid co-ion trapping on computationally accessible time scales.

211 The analysis of this approach will be presented in detail elsewhere.

212 D. Effect of finite pore length, and pore entrance and closing

213 We have pointed out in Section IV A that the pore entrance and closing influence the
 214 in-pore structure of ions, particularly strongly at non-zero voltages (Fig. 3). Figure 6a shows
 215 that this behaviour remains true also for long pores ($l = 20\text{nm}$), *i.e.*, the counter-ion density
 216 is systematically higher at the pore end and correspondingly lower where it begins; we note
 217 that these ion density profiles persist for long simulation runs (up to 200ns) and are likely the

²¹⁸ equilibrium profiles. Such a behaviour is understandable because image forces are weaker
²¹⁹ at the entrance, where the conducting pore walls end; in contrast, near the pore end the
²²⁰ additional (closing) surface amplifies the image-force effects and hence attracts more ions.
²²¹ As a result, the counter-ion density along the pore changes approximately linearly between
²²² these two points.

²²³ Interestingly, the MC simulations predict the counter-ion densities that are closer to those
²²⁴ at the pore end, rather than at the entrance (at the same applied potentials and for the same
²²⁵ densities at zero potential). The exact reason for this is not clear to us, but it is tempting
²²⁶ to speculate that it is actually the pore entrance that reduces the ion density, and in this
²²⁷ way affects the ion concentration in the whole pore and hence its charging behaviour. On
²²⁸ the other hand, it is also possible that the atomistic pore-wall structure in the MD model
²²⁹ induces a weak ordering of an ionic liquid, and thus leads to an additional entropic cost for
²³⁰ dense ion packing (recall that the pore walls in the MC model are flat). This implies that in
²³¹ the MD model a higher voltage is needed to induce the same counter-ion density as in the
²³² MC model, and this is indeed what we observe (*cf.* Fig. 7). It is worth noting that similar
²³³ effects have been reported for ionic liquids at flat (non-porous) electrodes [49].

²³⁴ This inhomogeneity of the ion distribution manifests itself in the accumulated charge
²³⁵ ($Q_{\text{whole-pore}}$), which depends sensitively on the pore length and shows a non-monotonic
²³⁶ behaviour (squares in Fig. 6b). Interestingly, $Q_{\text{whole-pore}}$ decreases as l increases (for long
²³⁷ pores), which is because the ion density at the pore entrance becomes less affected by the
²³⁸ pore closing, attending a lower value (Fig. 6a). Since the effects due to the pore closing
²³⁹ and opening weaken with increasing l , $Q_{\text{whole-pore}}$ approaches $Q_{\text{pore-middle}}$ as $l \rightarrow \infty$, where
²⁴⁰ $Q_{\text{pore-middle}}$ takes into account only the middle part of a pore. However, both $Q_{\text{pore-middle}}$
²⁴¹ and $Q_{\text{whole-pore}}$ are smaller than Q_{MC} obtained within the MC model featuring an infinitely
²⁴² long pore. As discussed, this is likely due to the effect that the pore entrance has on the
²⁴³ in-pore ion density (Fig. 6a).

²⁴⁴ Thus, Fig. 6 demonstrates that *there is no well-defined bulk region inside the pore*, where
²⁴⁵ the average ion density would be constant along the pore. This behaviour affects the charging
²⁴⁶ behaviour and hinders a direct *quantitative* comparison between the MC and MD models.
²⁴⁷ We therefore restrict further discussions mainly to qualitative comparisons.

²⁴⁸ **V. COMPARISON OF THE RESULTS FOR FINITE AND INFINITE PORES**

²⁴⁹ We are now in position to compare the simulation results of the MD and MC models with
²⁵⁰ finite and infinitely long nanopores, respectively. In the MD simulations, we have taken a
²⁵¹ voltage ramp of $k = 0.25\text{V/ns}$ whenever necessary (at voltages $\lesssim 2\text{V}$ we observe no trapping
²⁵² for the pore length considered); the size of a bulk region was $H = 80\text{\AA}$. The pore length was
²⁵³ $l = 80\text{\AA}$, but only the middle region of size 25\AA was used to analyse the results (this is to
²⁵⁴ exclude the contribution from strong ionic-liquid layering at the pore ends and entrances).

²⁵⁵ Since in MD simulations we had to adjust the ICC* charges each simulation step to
²⁵⁶ keep a constant potential on the electrode surfaces, these *constant-potential* simulations
²⁵⁷ are computationally demanding, and we have performed them only for a limited number
²⁵⁸ of voltages. As a result, since the differential capacitance and the charging parameter X_D
²⁵⁹ (see below) require numerical differentiations with respect to voltage, we have calculated
²⁶⁰ them with lower resolutions. This can be contrasted with our MC simulations, in which the
²⁶¹ metallic nature of the electrodes is taken into account via the interaction potentials (2) and
²⁶² (3). This allows to reduce the computational costs significantly (note that such analytical
²⁶³ solutions exist only for a few simple geometries [50]).

²⁶⁴ **A. Pore filling and charging mechanisms**

²⁶⁵ Figure 7 shows the total ion packing fraction $\eta_{\text{in-pore}}$ as a function of the applied po-
²⁶⁶ tential, and demonstrates that pore filling proceeds similarly in the MC and MD models.
²⁶⁷ Interestingly, in all cases of *strongly ionophilic* pores, *i.e.*, the pores with a substantial
²⁶⁸ amount of an ionic liquid at no voltage, $\eta_{\text{in-pore}}$ first decreases for increasing voltage, and
²⁶⁹ starts to increase only when there are no co-ions left in the pore. In other words, at low
²⁷⁰ voltages charging is dominated by *co-ion desorption*, while it is the *counter-ion adsorption*
²⁷¹ that drives charging at higher applied potentials [7, 14, 15, 46]. This is in agreement with
²⁷² the recent observation [46] showing that desorption (and swapping) are thermodynamically
²⁷³ preferable over adsorption in most cases, except of a narrow window of parameters in which
²⁷⁴ desorption and swapping are infeasible due to the lack of co-ions.

To characterize charging mechanisms in more detail, we introduce a charging parameter,

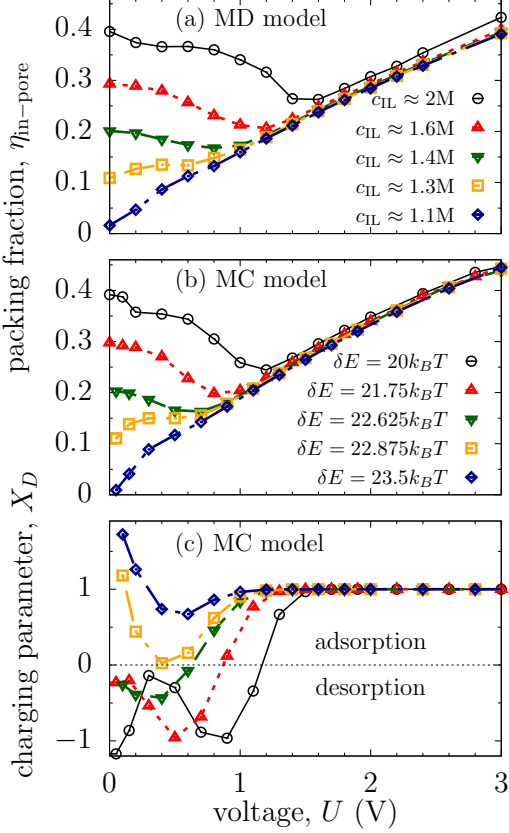


FIG. 7. Total packing fraction $\eta_{\text{in-pore}}$ of ions in a pore and charging parameter X_D from (a) MD and (b-c) MC simulations. Transfer energies (δE) and the ionic liquid concentrations (c_{IL}) have been matched such as to have approximately the same $\eta_{\text{in-pore}}$ at zero voltage. MC and MD models predict similar behaviours of $\eta_{\text{in-pore}}$ at low and intermediate voltages. Small discrepancies appear only at higher potentials likely due to the differences in the pore wall structures in the MD and MC models. (c) Charging parameter X_D , Eq. (4), obtained from MC simulations shows the regions where charging is dominated by adsorption ($X_D > 0$) and desorption ($X_D < 0$). $X_D = 0$ corresponds to swapping of co-ions for counterions. The same symbols and line codes are used in (c) as in (b). The comparison of X_D obtained within the MC and MD models is shown in Supplementary Fig. S5.

similar to the parameter X of Forse *et al.* [51],

$$X_D(U) = \frac{e}{C(U)} \frac{dN}{dU}, \quad (4)$$

where e is the elementary charge, $C(U) = dQ/dU$ the differential capacitance, Q denotes the accumulated charge and N the total number of ions. X_D expresses how charging is

related to pore filling or de-filling, and thus describes which charging mechanism takes place. If charging is driven solely by swapping of coions for counter-ions, then the total ion density does not change, $N = \text{const}$, and hence $X_D = 0$. For pure electrosorption we have $edN/dU = dQ/dU$ and thus $X_D = 1$, while for desorption $dQ/dU = -edN/dU$ and so $X_D = -1$. The parameter X of Forse *et al.* is related to X_D in a similar fashion as the integral capacitance is related to the differential capacitance, *i.e.*,

$$X(U) = \frac{1}{Q} \int_0^U X_D(u) C(u) du, \quad (5)$$

which can be seen as a voltage-averaged X_D with the weight $C(u)$, where $Q = \int_0^U C(u) du$ is a normalization constant.

The charging parameter X_D obtained from MC simulations is presented in Fig. 7c. It shows that at high voltages charging is solely due to counter-ion adsorption, *i.e.*, $X_D \approx 1$, but at low voltages it can be either co-ion desorption or counter-ion adsorption, depending on the transfer energy δE . Interestingly, for high values of δE , *i.e.*, when the pore is nearly empty at no applied potential, the parameter X_D is significantly greater unity, which means that *both* counter and co-ions are adsorbed into the pore at low voltages. This is likely because the additional ‘ion pairs’ screen the interactions between the counter-ions, reducing the thermodynamic cost of adsorption (note that at low densities the entropic cost of ion insertion is low).

286 B. Charging and differential capacitance

Figure 8 compares the accumulate charge $Q(U)$ from MC and MD simulations for pores with different occupancies at zero voltage, and demonstrates that also the charging process proceeds similarly in the MC and MD models. Interestingly, $Q(U)$ is practically independent of the transfer energies δE (MC simulations) and ionic liquid concentrations c_{IL} (MD simulations). This is because the electrostatic contribution ($\pm eU$) to the total electrochemical potential dominates the contribution due to δE and c_{IL} , respectively (see Section IV B).

Fine details of the charging process are captured by the differential capacitance $C = dQ/dU$. Although $Q(U)$ does not seem to vary significantly with δE (Fig. 8b), $C(U)$ shows nevertheless a complex behaviour, particularly for densely populated ionophilic pores. For such pores, the capacitance exhibits a first maximum corresponding to the co-ion/counter-

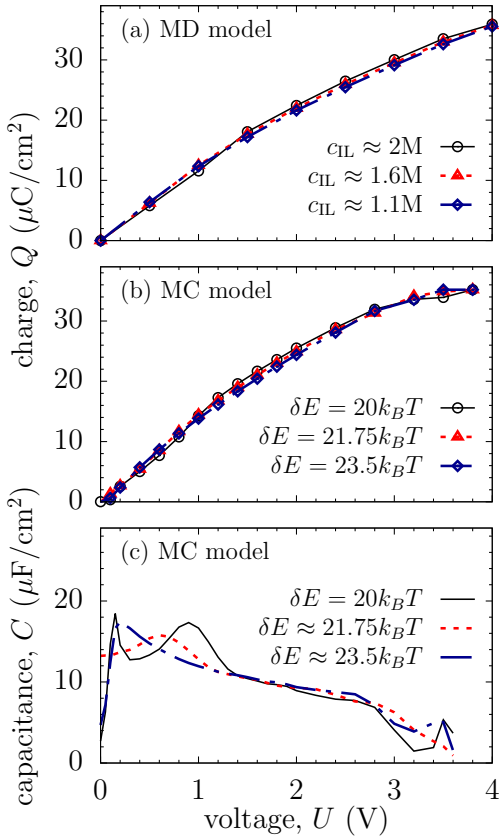


FIG. 8. Charging from MC and MD simulations. (a) Accumulated charge Q as a function of applied potential U from MD simulations for a few values of the total ionic liquid concentration c_{IL} in a supercapacitor. (b) Q from MC simulations for a few values of the transfer energy δE . We have adjusted δE and c_{IL} to give approximately the same in-pore ion packing fractions at zero voltage (see Fig. 2). For a detailed comparison of the $Q(V)$ curves see Fig. 10b and Supplementary Fig. S6. (c) Differential capacitance C as a function of voltage from MC simulations. The comparison of the capacitances obtained within the MC and MD models is shown in Supplementary Fig. S7.

297 ion swapping and a second maximum associated with the co-ion desorption, before it finally
 298 decreases as the pore becomes more and more occupied by counter-ions at high voltages. For
 299 weakly ionophobic pores there is only one maximum in $C(U)$ at low pore occupancies, while
 300 at high potentials the charging proceeds similarly for all pores. For strongly ionophobic
 301 pores, the charging curves are shifted to higher voltages (Supplementary Fig. S8). However,
 302 we have not been able to obtain such ionophobic pores in the MD model by varying the
 303 ionic liquid concentration c_{IL} ; thus, we shall not discuss this case further in this work.

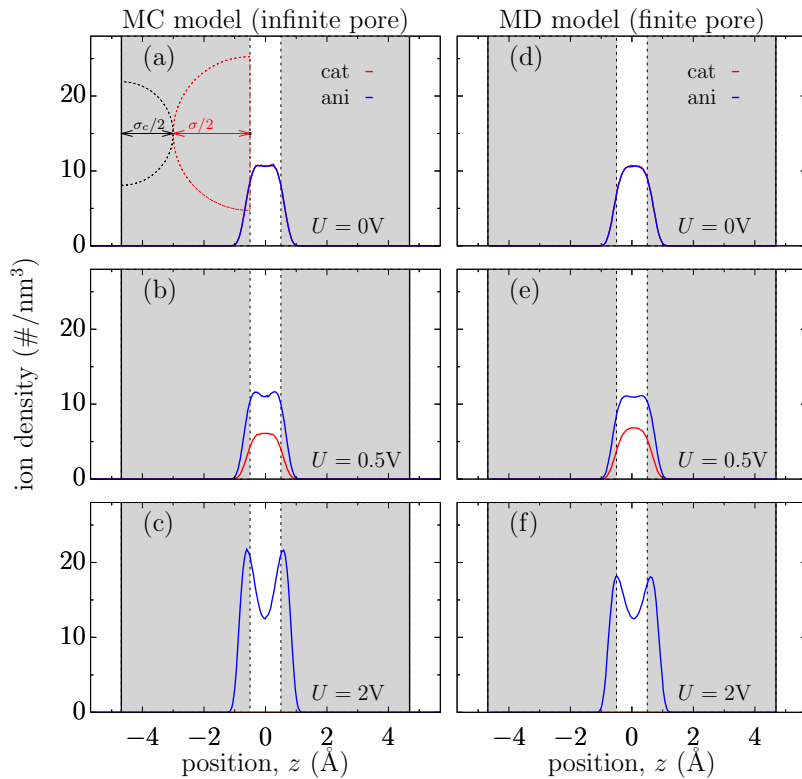


FIG. 9. Ion packing in narrow pores from (a-c) MC and (d-f) MD simulations. The transfer energy in (a-c) is $\delta E_{\pm} = 21.75k_B T$. In (d-f) the molar concentration of an ionic liquid is $c_{IL} \approx 1.635M$. The remaining parameters are the same as in Figs. 7 and 8.

304 Although charging in the MC and MD models show the same qualitative behaviour,
 305 there are some quantitative differences (Fig. 8a-b, and Supplementary Fig. S6 and S7), as
 306 discussed in Section IV D.

C. Ion structure

308 We have also looked at the ion structure across the pore. This is shown in Fig. 9, where we
 309 compare the density profiles obtained from MC and MD simulations for different voltages.
 310 The agreement is very good; small discrepancies are because we could not match exactly
 311 the ion densities at zero voltage.

312 At zero voltage the ion density has a maximum at the middle of the pore. This might
 313 seem surprising at first glance, since the image-force wall-ion attraction exhibits a *maximum*
 314 at the pore center (Fig. 1d). However, for ultranarrow pores considered in this work, this

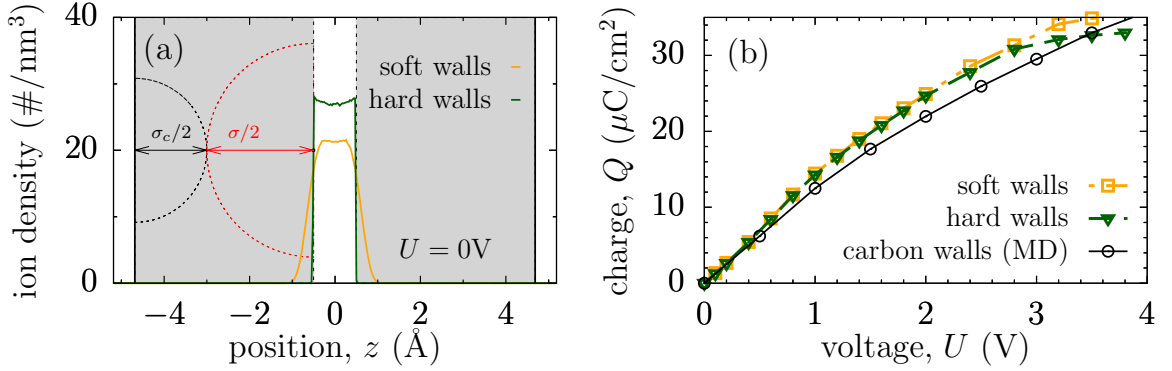


FIG. 10. Effect of pore walls. (a) Ion density profiles across the pore in the case of the hard and soft pore walls at zero applied voltage. For the profiles at non-zero voltages see Supplementary Fig. S9. (b) Accumulated charge as a function of applied voltage for pores with hard and soft walls obtained from MC simulations. The case of carbon walls (MD simulations) is shown for comparison. The ion transfer energies are $(\delta E)_{\text{hard}} = 21.5k_B T$ and $(\delta E)_{\text{soft}} = 21.75k_B T$ for the hard and soft pore walls, respectively; their values have been chosen such that the ion packing fraction $\eta_{\text{in-pore}} \approx 0.3$ in the non-polarised pores.

is altered by the wall-ion repulsive van-der Waals interactions, which produce a minimum rather than a maximum in the total wall-ion interaction potential (Supplementary Fig. S3). Nevertheless, at high applied potentials, the counter-ions prefer to locate themselves at the pore walls. This is because the electrostatic energy ($\sim eU$) dominates the unfavourable van der Waals interactions between the walls and the ions, while the increased ion density pushes the counter-ions closer to the walls.

321

VI. EFFECT OF PORE WALLS

In addition to the soft pore walls, which interact with the ions via Eq. (1), we have considered the model of *hard* walls, which are widely used in the literature [8, 23–27]. Figure 10 shows that the hard walls strongly influence the ionic liquid structure inside a pore, but their effect on the charge storage is moderate. For low voltages, the accumulated charge in both systems practically coincides, and the only significant differences arise at high applied potentials, where the pore with hard walls saturates while the soft-wall pore can accommodate more charge.

³²⁹ We have also considered the soft walls with the standard 9-3 Lennard-Jones interaction
³³⁰ potential between the walls and the ions. This interaction potential is more difficult to
³³¹ fit to the average interaction potential between the ions and the atomistic wall of the MD
³³² model, which is not very surprising. We have found that the in-pore ion structure depends
³³³ sensitively on the fitting parameters (results not shown). However, as in the case of the hard
³³⁴ walls, it has no significant effect on the charging behaviour.

³³⁵ We can conclude that although fine details of the non-electrostatic wall-ion interactions
³³⁶ are important for the ion structure, their impact on charging is minor, at least at low and
³³⁷ intermediates voltages.

³³⁸ **VII. CONCLUSIONS**

³³⁹ We have studied charge storage in supercapacitors with slit narrow pores using two mod-
³⁴⁰ els. In one model, treated by MD simulations, a supercapacitor consisted of two electrodes,
³⁴¹ each with a slit pore of a *finite* length. In the second model, we focused on a single pore,
³⁴² *infinitely* extended in the lateral directions; this model was studied grand-canonically by MC
³⁴³ simulations (Fig. 1). Our main conclusion is that although these two models are *qualitatively*
³⁴⁴ consistent with each other (Figs. 7, 8 and 9), there are some important differences due to the
³⁴⁵ finite pore length. In particular, the pore entrances and closings seem to have a vivid effect
³⁴⁶ on the ion structure inside a pore. At high concentrations and/or high applied potentials,
³⁴⁷ the ion density is not constant along the pore but varies roughly linearly between the pore
³⁴⁸ entrance and the pore end, where it exhibit a strongly oscillatory structure (Fig. 6). This
³⁴⁹ impedes a direct *quantitative* comparison of the two models.

³⁵⁰ We have also shown that:

- ³⁵¹ • In the MD model with finite pores, the ion density ρ_{bulk} between the electrodes of a
³⁵² supercapacitor can vary appreciably with the applied voltage. This can be corrected
³⁵³ by calibrating ρ_{bulk} during equilibration runs, to keep it constant, as in the single-pore
³⁵⁴ MC model. However, this change in the bulk density seems to have a minor effect
³⁵⁵ on the charging behaviour (Fig. 4). This result means that it is safe to consider rela-
³⁵⁶ tively small electrode-electrode separations in supercapacitor models and refrain from
³⁵⁷ computationally expansive bulk calibrations. Note that the studies of the charging
³⁵⁸ dynamics would not be straightforward if the bulk calibration were necessary.

- 359 • At intermediate and high voltages (and for long pores), the co-ions become trapped in
 360 the pores on our typical simulation time scales ($\sim 100\text{ns}$), producing non-equilibrium
 361 states. We have overcome this difficulty by using a voltage-ramp charging, instead of
 362 an abrupt step-voltage charging typically used in simulations (Fig. 5).

363 As co-ion trapping is expected to occur in experimental systems as well, we have stud-
 364 ied this problem in more detail. In particular, we worked out a method to accelerate
 365 charging in systems with co-ion trapping and determined optimal charge/discharge
 366 regimes; the results of this study will be presented in a separate article.

- 367 • At high voltages, charging proceeds exclusively via counter-ion adsorption, while at
 368 low voltages the charging process is dominated by either co-ion desorption or counter-
 369 ion adsorption, depending on the ion transfer energy or the total ion concentration
 370 (Fig. 7). Remarkably, at high transfer energies, implying low ion concentrations, both
 371 counter and co-ions are adsorbed into the pore at low voltages (the charging parameter
 372 $X_D > 1$, see Eq. (4) and Fig. 7c).
- 373 • Interestingly, the accumulated charge seems to be only weakly dependent on the total
 374 ions density in a supercapacitor (Fig. 8). This observation provides an additional de-
 375 gree of freedom for optimizing the charging dynamics by varying the ion concentration
 376 without significantly compromising the energy density (note that the fine details of
 377 the charging process are resolved by the differential capacitance, which does depend
 378 on the total ion concentration/ion transfer energy, Fig. 8c).
- 379 • Even though hard and soft pore walls lead to significant differences in the in-pore
 380 ion structure, they show practically the same charging behaviour (Fig. 10). This is
 381 because the applied potential ‘overrules’ all fine details of the non-electrostatic wall-ion
 382 interactions and the resulting ionic liquid structure.

383 In the context of the recent studies on ionophobicity of pores, it is instructive to emphasize
 384 that the pore occupancy at zero voltage, which determines the pore ionophobicity, can
 385 be varied by changing the total ion concentration (c_{IL}) in a supercapacitor. However, by
 386 changing c_{IL} alone we could not achieve a state corresponding to strongly ionophobic pores,
 387 which provide high stored energies [35, 46, 52] and fast charging [53–55]. Thus, another
 388 method must be proposed to control effectively the ionophobicity of pores.

Finally, we have considered only a few aspects of modeling supercapacitors and restricted our attention to charged soft spheres as a model for ionic liquids. Our results on the pore walls suggest that non-electrostatic interactions and image forces can have a profound impact on the in-pore ion structure. It will thus be interesting and fruitful to understand the effects due to the differences in ionic liquid models [56, 57], and whether such simple and computationally inexpensive models can capture the charging behaviour correctly.

395

VIII. SUPPLEMENTARY MATERIAL

Supplementary figures show the ion-wall repulsive interaction potential (Fig. S1); the ion's self-energy across the pore (Fig. S2); the total wall-ion interaction potential (Fig. S3); the effect of calibration on the ion density and accumulated charge (Fig. S4); the comparison of the charging parameter X_D (see Eq. (4)) obtained within the MD and MC models (Fig. S5); the accumulated charge within the MD and MC models (Fig. S6); the differential capacitance within the MD and MC models (Fig. S7); the differential capacitance and stored energy from MC simulations (Fig. S8); and the ion density profiles across the pore for pores with soft and hard walls from MC simulations (Fig. S9).

404

ACKNOWLEDGMENTS

C.H. and K.B. acknowledge the Deutsche Forschungsgemeinschaft (DFG) through the cluster of excellence “Simulation Technology” and the SFB 716 for financial support. We are also grateful for the computing resources on the Cray XC40 (Hazel Hen) from the HLRS in Stuttgart. This project has received funding from the European Unions Horizon 2020 research and innovation programme under the Marie Skłodowska-Curie grant agreement No 734276 (S.K. contribution).

[1] J. R. Miller and P. Simon, “Materials science electrochemical capacitors for energy management,” *Science* **321**, 651–652 (2008).

[2] P. Simon and Y. Gogotsi, “Capacitive energy storage in nanostructured carbonelectrolyte systems,” *Acc. Chem. Res.* **46**, 1094–1103 (2013).

- 415 [3] E. Raymundo-Piñero, K. Kierczek, J. Machnikowski, and F. Béguin, “Relationship between
416 the nanoporous texture of activated carbons and their capacitance properties in different
417 electrolytes,” *Carbon* **44**, 2498–2507 (2006).
- 418 [4] J. Chmiola, G. Yushin, Y. Gogotsi, C. Portet, P. Simon, and P. L. Taberna, “Anomalous
419 increase in carbon capacitance at pore sizes less than 1 nanometer,” *Science* **313**, 1760 (2006).
- 420 [5] C. Largeot, C. Portet, J. Chmiola, P.-L. Taberna, Y. Gogotsi, and P. Simon, “Relation
421 between the ion size and pore size for an electric double-layer capacitor,” *J. Am. Chem. Soc.*
422 **130**, 2730–2731 (2008).
- 423 [6] S. Kondrat, C. R. Pérez, V. Presser, Y. Gogotsi, and A. A. Kornyshev, “Effect of pore size
424 and its dispersity on the energy storage in nanoporous supercapacitors,” *Energy Environ. Sci.*
425 **5**, 6474 (2012).
- 426 [7] S. Kondrat and A. Kornyshev, “Superionic state in double-layer capacitors with nanoporous
427 electrodes,” *J. Phys.: Condens. Matter* **23**, 022201 (2011).
- 428 [8] S. Kondrat, N. Georgi, M. V. Fedorov, and A. A. Kornyshev, “A superionic state in nano-
429 porous double-layer capacitors: insights from monte carlo simulations,” *Phys. Chem. Chem.
430 Phys.* **13**, 11359–11366 (2011).
- 431 [9] C. C. Rochester, A. A. Lee, G. Pruessner, and A. A. Kornyshev, “Interionic interactions in
432 electronically conducting confinement,” *ChemPhysChem* **16**, 4121 (2013).
- 433 [10] A. Goduljan, F. Juarez, L. Mohammadzadeh, P. Quaino, E. Santos, and W. Schmickler,
434 “Screening of ions in carbon and gold nanotubes – a theoretical study,” *Electrochim. Comm.*
435 **45**, 4851 (2014).
- 436 [11] L. Mohammadzadeh, A. Goduljan, F. Juarez, P. Quaino, E. Santos, and W. Schmickler,
437 “Nanotubes for charge storage towards an atomistic model,” *Electrochim. Acta* **162**, 11–16
438 (2015).
- 439 [12] J. Vatamanu, O. Borodin, and G. D. Smith, “Molecular dynamics simulations of atomically
440 flat and nanoporous electrodes with a molten salt electrolyte,” *Phys. Chem. Chem. Phys* **12**,
441 170 (2010).
- 442 [13] G. Feng and P. T. Cummings, “Supercapacitor capacitance exhibits oscillatory behavior as a
443 function of nanopore size,” *J. Phys. Chem. Lett.* **2**, 2859–2864 (2011).
- 444 [14] P. Wu, J. Huang, V. Meunier, B. Sumpter, and R. Qiao, “Voltage dependent charge storage
445 modes and capacity in sub-nanometer pores,” *J. Phys. Chem. Lett.* **3**, 1732–1737 (2012).

- 446 [15] J. Vatamanu, Z. Hu, D. Bedrov, C. Perez, and Y. Gogotsi, “Increasing energy storage in elec-
447 trochemical capacitors with ionic liquid electrolytes and nanostructured carbon electrodes,”
448 *J. Phys. Chem. Lett.* **4**, 2829 (2013).
- 449 [16] J. Vatamanu, M. Vatamanu, and D. Bedrov, “Non-faradic energy storage by room tempera-
450 ture ionic liquids in nanoporous electrodes,” *ACS nano* **9**, 5999 (2015).
- 451 [17] Y. Shim and H. J. Kim, “Nanoporous carbon supercapacitors in an ionic liquid: A computer
452 simulation study,” *ACS Nano* **4**, 2345 (2010).
- 453 [18] C. Merlet, B. Rotenberg, P. A. Madden, P.-L. Taberna, P. Simon, Y. Gogotsi, and M. Salanne,
454 “On the molecular origin of supercapacitance in nanoporous carbon electrodes,” *Nature Mater.*
455 **11**, 306 (2012).
- 456 [19] R. Burt, K. Breitsprecher, B. Daffos, P.-L. Taberna, P. Simon, G. Birkett, X. S. Zhao, C. Holm,
457 and M. Salanne, “Capacitance of nanoporous carbon-based supercapacitors is a trade-off be-
458 tween the concentration and the separability of the ions,” *J. Chem. Phys. Lett.* (2016).
- 459 [20] H.-Q. Li, J.-Y. Luo, X.-F. Zhou, C.-Z. Yu, and Y.-Y. Xia, “An ordered mesoporous carbon
460 with short pore length and its electrochemical performances in supercapacitor applications,”
461 *J. Electrochem. Soc.* **154**, A731–A736 (2007).
- 462 [21] B. Dyatkin, O. G. B. Malinovskiy, YuliyaZozulya, P. Simon, and Y. Gogotsi, “High ca-
463 pacitance of coarse-grained carbide derived carbon electrodes,” *J. Power Sources* **306**, 32–41
464 (2016).
- 465 [22] While the electrodes with long well-defined slit pores exist [58, 59], extended long pores might
466 not be present in some porous materials, such as CDCs, which consist of interconnected
467 networks of different pores (see *e.g.* Ref. [60]). However, although such a network can be
468 described as a collection of shorter pores, the ionic liquid is nevertheless mainly present deeply
469 in the porous carbons and far from the contact with the bulk electrolyte or pore closings. In
470 this sense, infinitely extended pores can still be considered as good models for these porous
471 materials too. We note, however, that such pore networks and surface roughness may lead to
472 less structured ionic liquid configurations inside the pores, which can influence the charging
473 behaviour.
- 474 [23] K. Kiyohara and K. Asaka, “Monte carlo simulation of porous electrodes in the constant
475 voltage ensemble,” *J. Phys. Chem. C* **111**, 15903–15909 (2007).

- 476 [24] K. Kiyoohara, T. Sugino, and K. Asaka, “Electrolytes in porous electrodes: Effects of the pore
477 size and the dielectric constant of the medium,” *J. Chem. Phys.* **132**, 144705 (2010).
- 478 [25] K. Kiyoohara, T. Sugino, and K. Asaka, “Phase transition in porous electrodes,” *J. Chem.*
479 *Phys.* **134**, 154710 (2011).
- 480 [26] D. E. Jiang, Z. H. Jin, and J. Z. Wu, “Oscillation of capacitance inside nanopores,” *Nano*
481 *Lett.* **11**, 5373–5377 (2011).
- 482 [27] D. Jiang and J. Wu, “Unusual effects of solvent polarity on capacitance for organic electrolytes
483 in a nanoporous electrode,” *Nanoscale* (2014), 10.1039/c4nr00046c.
- 484 [28] M. Dudka, S. Kondrat, A. Kornyshev, and G. Oshanin, “Phase behaviour and structure of
485 a superionic liquid in nonpolarized nanoconfinement,” *J. Phys.: Condens. Matter* **28**, 464007
486 (2016).
- 487 [29] A. A. Kornyshev, *Faraday Discuss.* **164**, 117–133 (2014).
- 488 [30] A. A. Lee, S. Kondrat, and A. A. Kornyshev, “Charge storage in conducting cylindrical
489 nanopores,” *Phys. Rev. Lett.* **113**, 048701 (2014).
- 490 [31] W. Schmickler, “A simple model for charge storage in a nanotube,” *Electrochim. Acta* **173**,
491 91–95 (2015).
- 492 [32] C. C. Rochester, S. Kondrat, G. Pruessner, and A. A. Kornyshev, “Charging ultra-nanoporous
493 electrodes with size-asymmetric ions assisted by apolar solvent,” *J. Phys. Chem. C* **120**, 16042
494 (2016).
- 495 [33] J. Wu and Z. Li, “Density-functional theory for complex fluids,” *Annu. Rev. Phys. Chem.* **58**,
496 85 (2007).
- 497 [34] J. D. Weeks, D. Chandler, and H. C. Andersen, “Role of repulsive forces in determining the
498 equilibrium structure of simple liquids,” *J. Chem. Phys.* **54**, 5237 (1971).
- 499 [35] A. A. Lee, D. Vella, A. Goriely, and S. Kondrat, “Capacitance-power-hysteresis trilemma in
500 nanoporous supercapacitors,” *Phys. Rev. X* **6**, 021034 (2016).
- 501 [36] M. G. Martin, <http://towhee.sourceforge.net/>.
- 502 [37] B. Widom, “Some topics in the theory of fluids,” *J. Chem. Phys.* **39**, 2808–2812 (1963).
- 503 [38] “Espresso - extensible simulation package for research on soft matter,” <http://espressomd.org>, visited on 07/28/2016.
- 505 [39] H. J. Limbach, A. Arnold, B. A. Mann, and C. Holm, “ESPResSo – an extensible simulation
506 package for research on soft matter systems,” *Comp. Phys. Comm.* **174**, 704–727 (2006).

- 507 [40] A. Arnold, O. Lenz, S. Kesselheim, R. Weeber, F. Fahrenberger, D. Roehm, P. Košovan,
508 and C. Holm, “ESPResSo 3.1 — Molecular Dynamics Software for Coarse-Grained Models,”
509 in *Meshfree Methods for Partial Differential Equations VI*, Lecture Notes in Computational
510 Science and Engineering, Vol. 89, edited by M. Griebel and M. A. Schweitzer (Springer, 2013)
511 pp. 1–23.
- 512 [41] A. Arnold and C. Holm, “MMM2D: a fast and accurate summation method for electrostatic
513 interactions in 2D slab geometries,” *Comp. Phys. Comm.* **148**, 327–348 (2002).
- 514 [42] S. Kesselheim, M. Sega, and C. Holm, “The ICC* algorithm: A fast way to include dielec-
515 tric boundary effects into molecular dynamics simulations,” arXiv preprint arXiv:1003.1271
516 (2010).
- 517 [43] A. Arnold, K. Breitsprecher, F. Fahrenberger, S. Kesselheim, O. Lenz, and C. Holm, “Efficient
518 algorithms for electrostatic interactions including dielectric contrasts,” *Entropy* **15**, 4569–4588
519 (2013).
- 520 [44] V. Ballenegger, J. J. Cerdà, O. Lenz, and C. Holm, “The optimal P3M algorithm for com-
521 puting electrostatic energies in periodic systems,” *Journal of Chemical Physics* **128**, 034109
522 (2008).
- 523 [45] W. H. Press, *Numerical recipes: the art of scientific computing* (Cambridge Univ Pr, 2007).
- 524 [46] S. Kondrat and A. Kornyshev, “Pressing a spring: What does it take to maximize the energy
525 storage in nanoporous supercapacitors?” *Nanoscale Horiz.* **1**, 45–52 (2016).
- 526 [47] H. Kato, K. Nishikawa, H. Murai, T. Morita, and Y. Koga, “Chemical potentials in aqueous
527 solutions of some ionic liquids with the 1-ethyl-3-methylimidazolium cation,” *J. Phys. Chem.*
528 **B** **112**, 13344–13348 (2008).
- 529 [48] A. J. Pak and G. S. Hwang, “Charging rate dependence of ion migration and stagnation in
530 ionic-liquid-filled carbon nanopores,” *J. Phys. Chem. C* **120**, 24560 (2016).
- 531 [49] K. Breitsprecher, K. Szuttor, and C. Holm, “Electrode models for ionic liquid-based capaci-
532 tors,” *J. Phys. Chem. C* **119**, 22445–22451 (2015).
- 533 [50] C. C. Rochester, A. A. L. G. Pruessner, and A. A. Kornyshev, “Interionic interactions in
534 conducting nanoconfinement,” *ChemPhysChem* **14**, 4121–4125 (2013).
- 535 [51] A. C. Forse, C. Merlet, J. M. Griffin, and C. P. Grey, “New perspectives on the charging
536 mechanisms of supercapacitors,” *J. Am. Chem. Soc* **138**, 5731–5744 (2016).

- 537 [52] C. Lian, H. Liu, D. Henderson, and J. Wu, “Can ionophobic nanopores enhance the energy
538 storage capacity of electric-double-layer capacitors containing nonaqueous electrolytes?” *J.
539 Phys.: Condens. Matter* **28**, 414005 (2016).
- 540 [53] S. Kondrat and A. Kornyshev, “Charging dynamics and optimization of nanoporous superca-
541 pacitors,” *J. Phys. Chem. C* **117**, 12399–12406 (2013).
- 542 [54] S. Kondrat, P. Wu, R. Qiao, and A. Kornyshev, “Accelerating charging dynamics in sub-
543 nanometre pores,” *Nature Materials* **13**, 387 (2014).
- 544 [55] A. A. Lee, S. Kondrat, G. Oshanin, and A. A. Kornyshev, “Charging dynamics of superca-
545 pacitors with narrow cylindrical nanopores,” *Nanotechnology* **25**, 315401 (2014).
- 546 [56] K. Breitsprecher, P. Košovan, and C. Holm, “Coarse grained simulations of an ionic liquid-
547 based capacitor I: density, ion size, and valency effects,” *Journal of Physics: Condensed Matter*
548 **26**, 284108 (2014).
- 549 [57] K. Breitsprecher, P. Košovan, and C. Holm, “Coarse grained simulations of an ionic liquid-
550 based capacitor II. Asymmetry in ion shape and charge localization,” *Journal of Physics:
551 Condensed Matter* **26**, 284114 (2014).
- 552 [58] X. Yang, C. Cheng, Y. Wang, L. Qiu, and D. Li, “Liquid-mediated dense integration of
553 graphene materials for compact capacitive energy storage,” *Science* **341**, 534–537 (2013).
- 554 [59] M. R. Lukatskaya, O. Mashtalir, C. E. Ren, Y. DallAgnese, P. Rozier, P. L. Taberna,
555 M. Naguib, P. Simon, M. W. Barsoum, and Y. Gogotsi, “Cation intercalation and high
556 volumetric capacitance of two-dimensional titanium carbide,” *Science* **341**, 1502 (2013).
- 557 [60] M. Oschatz, P. P. S. Doröfler, W. Nickel, P. Beaunier, J.-N. Rouzaud, C. Fischer, E. Brunner,
558 and S. Kaskel, “Nanostructure characterization of carbide-derived carbons by morphological
559 analysis of transmission electron microscopy images combined with physisorption and raman
560 spectroscopy,” *Carbon* **105**, 314–322 (2016).